Dark Matter Results from First 98.7 Days of Data from the PandaX-II Experiment

Andi Tan,[2] Mengjiao Xiao,[1,2] Xiangyi Cui,[1] Xun Chen,[1] Yunhua Chen,[3] Deqing Fang,[4] Changbo Fu,[1] Karl Giboni,[1] Franco Giuliani,[1] Haowei Gong,[1] Xuyuan Guo,[3] Ke Han,[1] Shouyang Hu,[5] Xingtao Huang,[6] Xiangdong Ji,[1,7,2,‡] Yonglin Ju,[8] Siao Lei,[1] Shaoli Li,[1] Xiaomei Li,[5] Xinglong Li,[5] Hao Liang,[5] Qing Lin,[1,§] Huaxuan Liu,[8] Jianglai Liu,[1,*] Wolfgang Lorenzon,[9] Yugang Ma,[4] Yajun Mao,[10] Kaixuan Ni,[1,‖] Xiangxiang Ren,[1] Michael Schubnell,[9] Manbin Shen,[3] Fang Shi,[1] Hongwei Wang,[4] Jimin Wang,[3] Meng Wang,[6] Qiuhong Wang,[4] Siguang Wang,[10] Xuming Wang,[1] Zhou Wang,[8] Shiyong Wu,[3] Xiang Xiao,[1] Pengwei Xie,[1,†] Binbin Yan,[6] Yong Yang,[1] Jianfeng Yue,[3] Xionghui Zeng,[3] Hongguang Zhang,[1] Hua Zhang,[8] Huanqiao Zhang,[5] Tao Zhang,[1] Li Zhao,[1] Jing Zhou,[5] Ning Zhou,[1,11] and Xiaopeng Zhou[10]

(PandaX-II Collaboration)

[1]*INPAC and Department of Physics and Astronomy, Shanghai Jiao Tong University, Shanghai Laboratory for Particle Physics and Cosmology, Shanghai 200240, China*
[2]*Department of Physics, University of Maryland, College Park, Maryland 20742, USA*
[3]*Yalong River Hydropower Development Company, Ltd., 288 Shuanglin Road, Chengdu 610051, China*
[4]*Shanghai Institute of Applied Physics, Chinese Academy of Sciences, 201800, Shanghai, China*
[5]*Key Laboratory of Nuclear Data, China Institute of Atomic Energy, Beijing 102413, China*
[6]*School of Physics and Key Laboratory of Particle Physics and Particle Irradiation (MOE), Shandong University, Jinan 250100, China*
[7]*Center of High Energy Physics, Peking University, Beijing 100871, China*
[8]*School of Mechanical Engineering, Shanghai Jiao Tong University, Shanghai 200240, China*
[9]*Department of Physics, University of Michigan, Ann Arbor, Michigan, 48109, USA*
[10]*School of Physics, Peking University, Beijing 100871, China*
[11]*Department of Physics, Tsinghua University, Beijing 100084, China*

(Received 26 July 2016; published 16 September 2016)

We report the weakly interacting massive particle (WIMP) dark matter search results using the first physics-run data of the PandaX-II 500 kg liquid xenon dual-phase time-projection chamber, operating at the China JinPing underground laboratory. No dark matter candidate is identified above background. In combination with the data set during the commissioning run, with a total exposure of 3.3×10^4 kg day, the most stringent limit to the spin-independent interaction between the ordinary and WIMP dark matter is set for a range of dark matter mass between 5 and 1000 GeV/c^2. The best upper limit on the scattering cross section is found 2.5×10^{-46} cm^2 for the WIMP mass 40 GeV/c^2 at 90% confidence level.

DOI: 10.1103/PhysRevLett.117.121303

Weakly interacting massive particles, WIMPs in short, are a class of hypothetical particles that came into existence shortly after the big bang. The WIMPs could naturally explain the astronomical and cosmological evidences of dark matter in the Universe. The weak interactions between WIMPs and ordinary matter could lead to the recoils of atomic nuclei that produce detectable signals in deep-underground direct detection experiments. Over the past decade, the dual-phase xenon time-projection chambers (TPC) emerged as a powerful technology for WIMP searches both in scaling up the target mass, as well as in improving background rejection [1–3]. LUX, a dark matter search experiment with a 250 kg liquid xenon target, has recently reported the best limit of 6×10^{-46} cm^2 on the WIMP-nucleon scattering cross section [4], with no positive signals observed. The PandaX-II experiment, a half-ton scale dual-phase xenon experiment at the China JinPing underground laboratory (CJPL), has recently reported the dark matter search results from its commissioning run (run 8, 19.1 live days) with a 5845 kg day exposure [5]. The data were contaminated with significant ^{85}Kr background. After a krypton distillation campaign in early 2016, PandaX-II commenced physics data taking in March 2016. In this Letter, we report the combined WIMP search results using the data from the first physics run from March 9 to June 30, 2016 (run 9, 79.6 live days) and run 8, with a total of 3.3×10^4 kg day exposure, the largest reported WIMP data set among dual-phase xenon detectors in the world to date.

The PandaX-II detector has been described in detail in Ref. [5]. The liquid xenon target consists of a cylindrical TPC with dodecagonal cross section (opposite-side distance 646 mm), confined by the polytetrafluoroethylene (PTFE) reflective wall, and a vertical drift distance of 600 mm defined by the cathode mesh and gate grid located

at the bottom and top. For each physical event, the prompt scintillation photons ($S1$) and the delayed electroluminescence photons ($S2$) from the ionized electrons are collected by two arrays of 55 Hamamatsu R11410-20 photomultiplier tubes (PMTs) located at the top and bottom, respectively. This allows reconstruction of an event energy and position. A skin liquid xenon region outside of the PTFE wall was instrumented with 48 Hamamatsu R8520-406 1-inch PMTs serving as an active veto. The γ background, which produces electron recoil (ER) events, can be distinguished from the dark matter nuclear recoil (NR) using the $S2$-to-$S1$ ratio.

During the data taking period in run 9, a few different TPC field settings were used at different running periods (Table I) to maximize the drift and electron extraction fields while avoiding spurious photons and electrons emission from the electrodes. In each period, calibration runs were taken to study the detector responses. The PMT gains were calibrated using the single photoelectrons (PEs) produced by the low-intensity blue-light pulses transmitted into the detector. To study the multiple PE production in R11410-20 by the approximately 178 nm photons in xenon [6], we measured the PE distributions for individual PMTs using low intensity (<3 PE) physical $S1$ signals. An average double PE fraction (DPF, defined as the ratio between the occurrence of double PE emission to the total occurrence of nonzero PEs) of 0.21 ± 0.02 was obtained. The position-dependent responses in $S1$ and $S2$ were calibrated using the 164 keV γ peak from metastable ^{131m}Xe, produced by exposure to cosmic rays at ground and neutrons during NR calibration. Towards the end of run 9, the electron lifetime reached 940 ± 50 μs, compared to the maximum electron drift time 350 μs in the TPC. The nonuniformities for $S1$ (3D) and $S2$ (horizontal plane) were both measured to be less than 10% in standard deviation in the fiducial volume (FV, defined later). The photon detection efficiency (PDE), the electron extraction efficiency (EEE), and the single electron gain (SEG) and their uncertainties are also shown in Table I.

TABLE I. Summary of four settings in run 9 where E_{drift} and E_{extract} are the drift field in the liquid and electron extraction field in the gaseous xenon, respectively. The field values were calculated based on a COMSOL simulation. The fractional uncertainties of the PDE, EEE, and SEG are 5%, 6%, and 3%, respectively, for all settings. Only the average electron lifetime is given in the table, although the $S2$ vertical uniformity correction was performed for every data taking unit, typically lasting for 24 hours, based on the electron lifetime obtained therein.

Setting	Live time (day)	E_{drift} (V/cm)	E_{extract} (kV/cm)	PDE (%)	EEE (%)	SEG PE/e	τ_e (μs)
1	7.76	397.3	4.56	11.76	46.04	24.4	348.2
2	6.82	394.3	4.86	11.76	54.43	26.9	393.1
3	1.17	391.9	5.01	11.76	59.78	26.7	409.0
4	63.85	399.3	4.56	11.76	46.04	24.4	679.6

The analysis reported in this Letter follows the procedure as in Ref. [5] with the following major differences. An improved position reconstruction was developed based on a data-driven photon acceptance function (PAF) similar to Ref. [7], leading to a better FV definition. We performed NR calibration runs using a low-intensity (approximately 2 Hz) ^{241}Am-Be (AmBe) neutron source with improved statistics, and an ER calibration run by injecting tritiated methane [8], leading to a better understanding of the distributions of the NR and ER events. A boosted-decision-tree (BDT) cut method was developed to suppress accidental background by more than a factor of 3. Together with a much larger exposure and lower Kr background, these improvements account for the much more sensitive dark matter search results reported here.

The data quality cuts used in this analysis follow those in Refs. [9] and [5], including noise filters on ripplelike waveforms, cuts on $S1$ and $S2$ to remove events with abnormal PMT pattern or top/bottom ratio, and a 3-PMT coincidence and no-more-than two "$S1$-like" signals per event requirement to suppress random coincidence.

Most of external background events are located close to the detector boundary; therefore, a powerful background rejection demands good position reconstruction. In addition to the template matching (TM) algorithm in Ref. [9], a new algorithm was developed based on an iterative fitting of the position-dependent PAF for each PMT. For PMTs located close to the PTFE wall, the PAFs took into account effects due to photon reflections. In each iteration, the position was reconstructed by maximizing the charge likelihood according to the PAF obtained from the previous iteration, and the new position entered into the determination of the next PAF. Using this reconstruction, the Kr events in run 8 and the tritium calibration events in run 9 yielded good uniformity in the horizontal plane.

The ER and NR calibration events through tritiated methane and AmBe sources are shown in $\log_{10}(S2/S1)$ vs $S1$ in Fig. 1 after the dark matter selection cuts (Table IV). The AmBe calibration was carried out in between the dark matter running periods. A full Monte Carlo (MC) simulation based on GEANT4 [10,11] (v10.2) including neutron-gamma correlated emission from the source, detailed detector geometry, neutron propagation in, and interactions with the detector (following the recommended physics list [12]), and $S1$-$S2$ signal production (NEST-1.0-based [13]) was developed to compare to the data. According to the simulation, less than 10% of the low energy events are contaminated with multiple scattering in the dead region ("neutron X"). The data quality cuts mentioned above further suppress the neutron-X events; therefore, the final sample was considered as a pure single-scatter NR sample at this stage. 3447 such events were collected for 6.8 days in total, with less than 1%

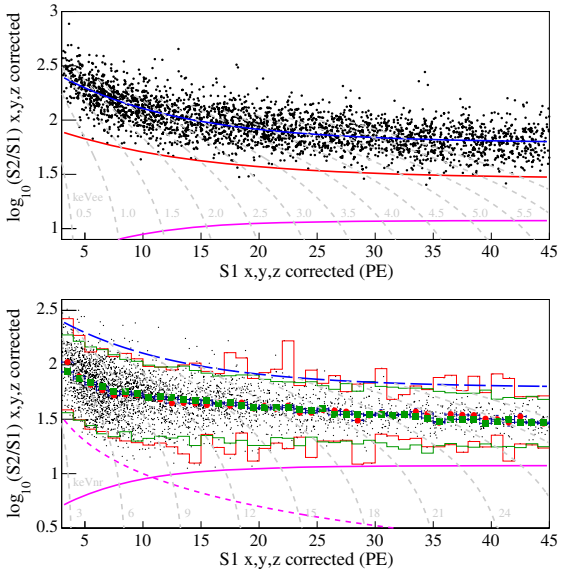

FIG. 1. Top: tritium calibration data in $\log_{10}(S2/S1)$ vs $S1$, and fits of medians of ER (blue) and NR (red) data. Bottom: AmBe calibration data in $\log_{10}(S2/S1)$ vs $S1$, together with medians from the data (red solid circles) and MC calculations (green squares), and the fit to ER medians (blue dashed). The 2.3 and 97.7 percentiles from the data (red lines) and MC calculations (green lines) are overlaid. The dashed magenta curve is the 100 PE selection cut for $S2$. In both panels, solid magenta curves represent the 99.9% NR acceptance curve from the MC calculations. The gray dashed curves represent the equal energy curves in ER and NR energy for the top and bottom panels, respectively.

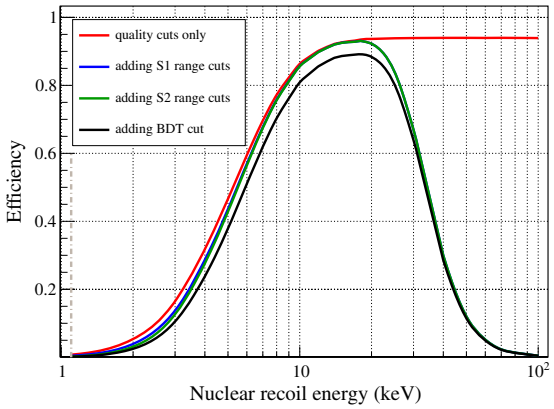

FIG. 2. The detection efficiencies as functions of the NR energy using untuned NEST model after successive applications of selections indicated in the legend. The BDT acceptance shown is determined by applying the BDT efficiency as a function of $S1$; the acceptance is virtually unchanged if the BDT efficiency is instead applied to $S2$. The dashed line at 1.1 keV_{nr} indicates the cutoff used in the WIMP limit setting.

contamination from the ER background. In the bottom panel of Fig. 1, the medians and widths of the NR data were compared to those obtained from the NEST-1.0 NR model [13] with detector parameters (PDE, EEE, SEG, and DPF) taken into account, and a good agreement is observed. The distributions in $S1$ and $S2$ were also compared to the MC calculation, a small discrepancy was observed in detailed shape for small $S1$ and $S2$. A tuning of the NEST model could improve the comparison (see Fig. 11 in Supplemental Material [14]) but worsen the agreement for medians of $\log_{10}(S2/S1)$ at low energy, which warrant further investigation. Following the standard practice, untuned NEST is used when reporting the official results. The corresponding efficiencies as functions of NR energy are shown in Fig. 2, which are later applied to calculate the dark matter detection efficiency.

At the end of run 9, tritiated methane with a specific activity of 0.1 mCi/mmol was administered into the detector through a liquid-nitrogen cold trap, a leak valve, and a 100 mL sample chamber under vacuum, which was flushed with xenon gas in the detector. We collected a total of 2807 tritium β-decay events. Among these, nine leaked below the median of the NR band, leading to a leakage fraction of $0.32\% \pm 0.11\%$.

During the krypton distillation campaign in early 2016, 1.1 ton of xenon was exposed to about one month of sea level cosmic ray radiation, leading to the production of ^{127}Xe, which then decayed via electron capture (EC) to ^{127}I producing characteristic ER energy deposition in the detector. The ^{127}Xe level was identified by the 33 keV K-shell x ray (following EC), with a decay rate of about 1.1 ± 0.3 and 0.1 ± 0.03 mBq/kg at the beginning and end of run 9, respectively. In the low-energy region, M-shell and L-shell vacancies of ^{127}I can produce 1.1 keV and 5.2 keV ER events in the detector, respectively. The background was estimated to be 0.37 ± 0.05 mDRU (1 mDRU $= 10^{-3}$ events/day/kg/keV_{ee} where keV_{ee} represents "electron equivalent" energy) below 10 keV_{ee} based on the MC calculations by scaling the measured K-shell x ray rate, in good agreement with 0.42 ± 0.08 and 0.40 ± 0.13 mDRU obtained from the spectrum fit and time-dependence fit of the low energy events. We chose 0.42 mDRU as the nominal value with a systematic uncertainty of 25%. The krypton background level was estimated *in situ* using the β-γ delayed coincidence from ^{85}Kr decay. In total, 52 candidates were identified in run 9 within 329 kg of FV (discussed later) and no time dependence was observed, leading to an estimate of 44.5 ± 6.2 ppt of Kr in xenon assuming a ^{85}Kr concentration of 2×10^{-11} in natural Kr. This represents a factor of 10 reduction compared to the Kr level in Ref. [5].

The backgrounds due to radioimpurity of detector components shall be the same as those in Ref. [5], and so is the neutron background. The ER background due to Rn was estimated *in situ* using the β-α and α-α delayed coincidence events. The ^{222}Rn and ^{220}Rn decays were estimated to be 8.6 ± 4.6 and 0.38 ± 0.21 μBq/kg, respectively, consistent with the results in Ref. [5]. We also estimated the background from the ^{136}Xe double-β decay events and neutrinos (see Ref. [17] and references therein).

TABLE II. Summary of ER backgrounds from different components in run 8 and run 9. The fractional uncertainties for ^{85}Kr and ^{127}Xe are 17% and 0% for run 8 and 14% and 25% for run 9, respectively. The uncertainties for ^{222}Rn and ^{220}Rn in both runs are taken to be 54% and 55%, respectively. The fractional uncertainty due to detector materials is estimated to be 50% based on the systematic uncertainty of the absolute efficiency of the gamma counting station. Different from Ref. [5], values in the table are now folded with detection efficiency.

Item	Run 8 (mDRU)	Run 9 (mDRU)
^{85}Kr	11.7	1.19
^{127}Xe	0	0.42
^{222}Rn	0.06	0.13
^{220}Rn	0.02	0.01
Detector material ER	0.20	0.20
Total	12.0	1.95

The former produces an ER background of 0.10 ± 0.01 events per 10 000 kg day. The neutrino ER background is dominated by pp solar neutrinos and is estimated to be between 0.2 and 6.0 events per 10 000 kg day where the lower and upper values assume zero or the current experimental limit of the neutrino magnetic moment [18], respectively. The neutrino NR background was estimated to be 1×10^{-3} events per 10 000 kg day. The final low energy background composition is summarized in Table II.

Similar to Ref. [9], the accidental background was computed by randomly pairing the isolated $S1$ (1.8 Hz) and $S2$ (approximately 1500/day) events within the dark matter selection range. The data quality cuts mentioned earlier suppressed this background to 33%, among which 15% is below the NR median. To optimize the rejection for such background, further cuts were developed based on the boosted-decision-tree (BDT) method [19], in which the below-NR-median AmBe calibration data and randomly paired $S1$-$S2$ signals were used as the input signal and background, respectively. The input data were split into two equal statistics sets, one for training and the other for test. The BDT cuts target, for example, events where the drift time and $S2$ width are inconsistent, or where the $S2$ shape indicates an $S2$ originating from the gate or gas regions. Thirteen variables entered into the training including the charge of $S1$, $S2$, and the drift time, the width, 10% width, rising slope, waveform asymmetry, and top/bottom ratio of the $S2$, ratio of maximum bottom channel to total, and top/bottom ratio of the $S1$, spikes within and spikes around the $S1$ (indicators of a $S2$ mis-ID), and the pre-$S2$ area in a window between 1.5 and 3 μs (tag of a gate event). After applying the BDT cuts to the accidental background surviving the data quality cuts, events below the NR median were strongly suppressed to 27%, while the overall AmBe NR efficiency was maintained at 93%. The uncertainty on the remaining accidental background was estimated to be 45% using the difference found in run 8 and run 9.

Similar to Ref. [5], the final $S1$ range cut was chosen to be between 3 to 45 PE, corresponding to an average energy window between 1.3 to 8.7 keV$_{ee}$ (4.6 to 35.0 keV$_{nr}$), and $S2$s were required to be between 100 PE (raw) and 10 000 PE (uniformity corrected). For all events with a single $S2$, the FV cut was determined based on the PAF-reconstructed position distribution. The selection criterion in the horizontal plane was taken to be $r < 268$ mm, using data with $S1$ outside of the dark matter search window (between 50 and 200 PE). The drift time was required to be between 18 to 310 μs, where the maximum drift time cut was to suppress the below-cathode γ energy deposition (so-called "gamma X") from ^{127}Xe decays. The liquid xenon mass was estimated to be 329 ± 16 kg, where the uncertainty was estimated based on the position difference between the PAF and TM methods, consistent with other estimates using the tritium event distribution and expected intrinsic resolution from the TM method. The vertical electric field deformation resulting from the accumulations of wall charges in the TPC [4] was estimated using the ^{210}Po plate-out events from the PTFE wall. The reconstructed positions are 2.4 mm (18 μs) to 6.3 mm (310 μs) away from the geometrical wall, a combined effect from reconstruction and field distortion. Therefore we have made a conservative choice of the FV and neglected the field deformation therein. Under these cuts, the final expected background budget is summarized in Table III.

The event rates of run 9 after successive selections are summarized in Table IV. The skin veto selections are more effective than that in run 8 since the background was less dominated by the volume-uniform ^{85}Kr β decays. The vertex distribution of all events before and after the FV cut is shown in Fig. 3. Outside the FV, pileup of events near the cathode, the gate, and the wall were observed. After the FV cut, 389 events survived, and event distribution in radius

TABLE III. The expected background events in run 8 and run 9 in the FV, before and after the NR median cut. The fractional uncertainties of expected events in the table are 17% (run 8 ER), 12% (run 9 ER), 45% (accidental), and 100% (neutron), respectively. Both the uncertainties from the ER rate and leakage fraction, $0.32\% \pm 0.11\%$, were taken into account in estimating the uncertainty of ER background below the NR median. Number of events from the data are shown in the last column.

	ER	Accidental	Neutron	Total expected	Total observed
Run 8	622.8	5.20	0.25	628 ± 106	734
Below NR median	2.0	0.33	0.09	2.4 ± 0.8	2
Run 9	377.9	14.0	0.91	393 ± 46	389
Below NR median	1.2	0.84	0.35	2.4 ± 0.7	1

TABLE IV. The event rates in run 9 after various analysis selections.

Cut	#Events	Rate (Hz)
All triggers	24502402	3.56
Single $S2$ cut	9783090	1.42
Quality cut	5853125	0.85
Skin veto cut	5160513	0.75
$S1$ range	197208	2.87×10^{-2}
$S2$ range	131097	1.91×10^{-2}
18 μs FV cut	21079	3.06×10^{-3}
310 μs FV cut	7361	1.07×10^{-3}
268 mm FV cut	398	5.79×10^{-5}
BDT cut	389	5.66×10^{-5}

square agree statistically with a flat distribution, indicating no effects from the electric field deformation due to wall charges. One event was found below the NR median curve, with its location indicated in Fig. 3. The $\log_{10}(S2/S1)$ vs $S1$ distribution for the 389 candidates is shown in Fig. 4. Being close to the NR median line, the single below-NR-median event is consistent with a leaked ER background.

The data in run 8 and run 9 were combined in the final analysis to obtain a new WIMP search limit. The run 8 data were reanalyzed with the updated reconstruction, and data selection cuts except that the vertical cuts were maintained from 20 to 346 μs (FV = 367 kg), since there was no gamma-X contamination from ^{127}Xe in run 8. This represents the largest dark-matter-search data set among dual-phase xenon detectors to date with an overall exposure of 3.3×10^4 kg day. A likelihood approach similar to that in Ref. [9] was used to fit the measured data distribution in $S1$ and $S2$. A parameterized tritium event distribution was used to simulate expected distributions for different ER background components, and that for accidentals was obtained from the data. The DM NR signals were simulated with the untuned NEST for different WIMP masses as the expected

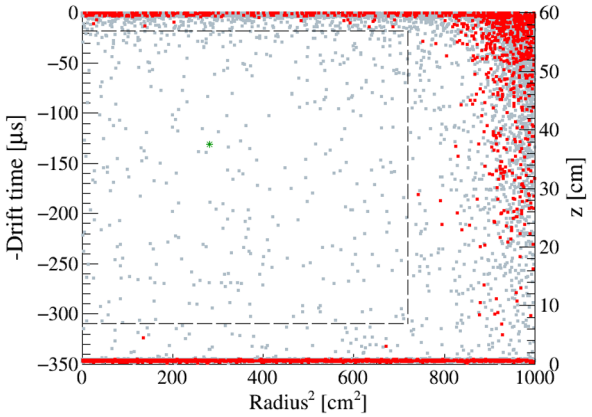

FIG. 3. Position distribution of events that pass all selections (gray points), and those below the NR median (outside FV: red points; inside FV: green star), with FV cuts indicated as the black dashed box.

DM distributions, with the conservative low energy cutoff at 1.1 keV$_{nr}$ [4]. The entire data set was separated into 15 time bins to take into account the time dependent factors such as the electron lifetime, the background level, and other detector parameters (Table I). The scales of all five background components, ^{127}Xe, ^{85}Kr, other ER background (including Rn and material background), accidental, and neutron background, were defined as global nuisance parameters with their corresponding Gaussian penalty terms constructed based on systematic uncertainties in Tables II and III. The nominal rates for the latter four backgrounds were taken from Table II, and for ^{127}Xe, the nominal rate was derived from the table to include the time dependence. The uncertainties for PDE, EEE, and SEG in the caption of Table I were verified to have small impact to the results and were neglected in the likelihood fit for simplicity.

To obtain the exclusion limit to spin-independent isoscalar WIMP-nucleon cross section, profile likelihood ratio [20,21] was constructed over grids of WIMP mass and cross section, and the final 90% confidence level (C.L.) cross section upper limits were calculated using the so-called CL$_s$ approach [22,23]. The final results are shown in Fig. 5, with results from XENON100 [15], PandaX-II run 8 [5] and LUX [4] overlaid. Our upper limits lie within the $\pm 1\sigma$ sensitivity band, consistent with statistical expectation based on Table III. The lowest cross section limit obtained is 2.5×10^{-46} cm^2 at a WIMP mass of 40 GeV/c^2, which represents an improvement of more than a factor of 10 from Ref [5]. In the high WIMP mass region, our results are more than a factor of 2 more stringent than the LUX results [4]. Note that we have been generally conservative in officially reporting the first limits in this Letter. WIMP NR

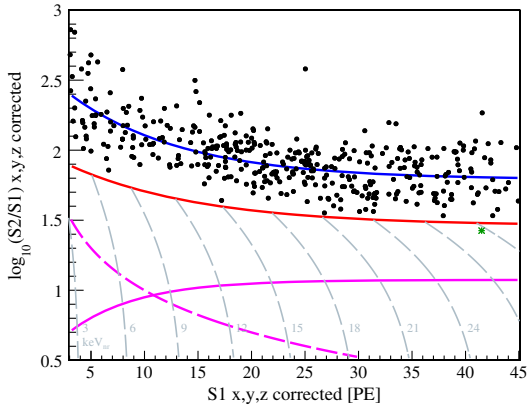

FIG. 4. The distribution of $\log_{10}(S2/S1)$ versus $S1$ for the dark matter search data. The median of the NR calibration band is indicated as the red curve. The dashed magenta curve represents the equivalent 100 PE cut on $S2$. The solid magenta curve is the 99.99% NR acceptance curve. The gray dashed curves represent the equal energy curves with NR energy indicated in the figures. The data point below the NR median curve is highlighted as a green star.

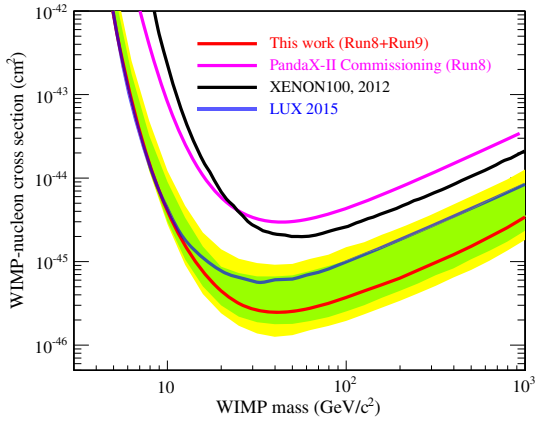

FIG. 5. The 90% C.L. upper limits for the spin-independent isoscalar WIMP-nucleon cross sections from the combination of PandaX-II run 8 and run 9 (red solid). Selected recent world results are plotted for comparison: PandaX-II run 8 results [5] (magenta), XENON100 225 day results [15] (black), and LUX 2015 results [4](blue). The 1 and 2-σ sensitivity bands are shown in green and yellow, respectively.

modeling with a tuned NEST could result in an even more stringent limit (see Fig. 16 in Supplemental Material [14]), and a more elaborated treatment of FV cuts would also help.

In conclusion, we report the combined WIMP search results using data from run 8 and run 9 of the PandaX-II experiment with an exposure of 3.3×10^4 kg day. No dark matter candidates were identified above background and 90% upper limits were set on the spin-independent elastic WIMP-nucleon cross sections with a lowest excluded value of 2.5×10^{-46} cm^2 at a WIMP mass of 40 GeV/c^2, the world's best reported limit so far. The result is complementary to the searches performed at the LHC, which have produced various WIMP-nucleon cross section limit in the range from 10^{-40} to 10^{-50} (cf. Refs. [24] and [25]), dependent on the dark matter production models. The PandaX-II experiment continues to take physics data to explore the previously unattainable WIMP parameter space.

This project has been supported by a 985-III grant from Shanghai Jiao Tong University, grants from National Science Foundation of China (Grants No. 11435008, No. 11455001, No. 11505112, and No. 11525522), a grant from the Ministry of Science and Technology of China (Grant No. 2016YFA0400301), and a grant from the Office of Science and Technology in Shanghai Municipal Government (Grant No. 11DZ2260700). This work is supported in part by the Chinese Academy of Sciences Center for Excellence in Particle Physics (CCEPP). The project is also sponsored by Shandong University, Peking University, and the University of Maryland. We also would like to thank Dr. Xunhua Yuan and Chunfa Yao of China Iron and Steel Research Institute Group, and we are particularly indebted to Director De Yin from Taiyuan Iron and Steel (Group) Co. LTD for crucial help on nuclear-grade steel plates. We also thank C. Hall for helping with specifics of tritium calibration. Finally, we thank the following organizations and personnel for indispensable logistics and other supports: the CJPL administration including directors Jianping Cheng and Kejun Kang and manager Jianmin Li, and the Yalong River Hydropower Development Company Ltd.

Note added.—As this manuscript is in the final production stage, a paper was submitted to the arXiv by the LUX collaboration on their dark matter search results with a similar exposure, which placed slightly stronger upper limit on the WIMP-nucleon cross section at 2.2×10^{-46} cm^2 for a WIMP mass of 50 GeV/c^2 (see [26]).

*Corresponding author.
jianglai.liu@sjtu.edu.cn.
†Corresponding author.
willandy@sjtu.edu.cn.
‡PandaX-II Collaboration Spokesperson.
xdji@sjtu.edu.cn.
§Present address: Department of Physics, Columbia University.
‖Present address: Department of Physics, University of California, San Diego.

[1] E. Aprile, C. E. Dahl, L. de Viveiros, R. Gaitskell, K. L. Giboni, J. Kwong, P. Majewski, K. Ni, T. Shutt, and M. Yamashita, Phys. Rev. Lett. **97**, 081302 (2006).
[2] E. Aprile *et al.* (XENON100), Phys. Rev. Lett. **109**, 181301 (2012).
[3] D. Yu. Akimov *et al.*, Phys. Lett. B **709**, 14 (2012).
[4] D. S. Akerib *et al.* (LUX), Phys. Rev. Lett. **116**, 161301 (2016).
[5] A. Tan *et al.* (PandaX), Phys. Rev. D **93**, 122009 (2016).
[6] C. H. Faham, V. M. Gehman, A. Currie, A. Dobi, P. Sorensen, and R. J. Gaitskell, J. Instrum. **10**, P09010 (2015).
[7] V. Solovov, V. Belov *et al.*, IEEE Trans. Nucl. Sci. **59**, 3286 (2012).
[8] D. S. Akerib *et al.* (LUX), Phys. Rev. D **93**, 072009 (2016).
[9] X. Xiao *et al.* (PandaX), Phys. Rev. D **92**, 052004 (2015).
[10] S. Agostinelli *et al.* (GEANT4), Nucl. Instrum. Methods Phys. Res., Sect. A **506**, 250 (2003).
[11] J. Allison *et al.*, IEEE Trans. Nucl. Sci. **53**, 270 (2006).
[12] http://geant4.cern.ch/support/proc_mod_catalog/physics_lists/useCases.shtml.
[13] B. Lenardo, K. Kazkaz, M. Szydagis, and M. Tripathi, IEEE Trans. Nucl. Sci. **62**, 3387 (2015).
[14] Supplmental Material at for PandaX-II first data results, see http://link.aps.org/supplemental/10.1103/PhysRevLett.117.121303, which includes Refs. [4,5,15,16].
[15] E. Aprile *et al.* (XENON100), Phys. Rev. Lett. **111**, 021301 (2013).

[16] E. A. Bagnaschi *et al.*, Eur. Phys. J. C **75**, 500 (2015).
[17] J. Billard, E. Figueroa-Feliciano, and L. Strigari, Phys. Rev. D **89**, 023524 (2014).
[18] A. G. Beda, V. B. Brudanin, V. G. Egorov, D. V. Medvedev, V. S. Pogosov, E. A. Shevchik, M. V. Shirchenko, A. S. Starostin, and I. V. Zhitnikov, Phys. Part. Nucl. Lett. **10**, 139 (2013).
[19] B. P. Roe, H.-J. Yang, J. Zhu, Y. Liu, I. Stancu, and G. McGregor, Nucl. Instrum. Methods Phys. Res., Sect. A **543**, 577 (2005).
[20] G. Cowan, K. Cranmer, E. Gross, and O. Vitells, Eur. Phys. J. C **71**, 1554 (2011); **73**, 2501(E) (2013).
[21] E. Aprile *et al.* (XENON100), Phys. Rev. D **84**, 052003 (2011).
[22] A. L. Read, J. Phys. G **28**, 2693 (2002).
[23] T. Junk, Nucl. Instrum. Methods Phys. Res., Sect. A **434**, 435 (1999).
[24] G. Aad *et al.* (ATLAS), J. High Energy Phys. 11 (2015) 206.
[25] G. Aad *et al.* (ATLAS), Eur. Phys. J. C **75**, 299 (2015); **75**, 408(E) (2015).
[26] D. S. Akerib *et al.*, arXiv:1608.07648.